Journal of Sound and Vibration (1994) **169**(4), 459–483

HIGH SPEED STABILITY OF COUPLED BAND/WHEEL SYSTEMS: THEORY AND EXPERIMENT

S.-J. HWANG AND N. C. PERKINS

Department of Mechanical Engineering and Applied Mechanics, The University of Michigan, Ann Arbor, Michigan 48109-2125, *U.S.A.*

(*Received* 3 *January* 1992, *and in final form* 22 *July* 1992)

A theoretical model is derived that describes the planar, non-linear response of a continuous band circulating about two rotating wheels. A closed form analysis of the non-linear steady response leads to elliptic integral solutions for the equilibrium band geometry and tension. These solutions, which are evaluated over a wide range of band/wheel designs, are also used to evaluate the extent of band/wheel contact and the effect of self-equilibriating wheel torques. The equations of motion are linearized about the equilibrium solution, and equilibrium stability and the free linear response are predicted from a discretized model. Results of a companion experimental study support theoretical predictions of steady and dynamic response. In particular, results indicate that band/wheel systems maintain stability at high translation speeds.

1. INTRODUCTION

Band/wheel systems, composed of a continuous band drawn under tension about two supporting wheels, belong to a class of mechanical systems referred to as *axially moving materials* [1]. Other axially moving material systems include belt and chain drives, thread and fibers winders, paper handling machinery, magnetic tape recording devices and cable pay-out/reel-in systems. The features common to all axially moving material systems are discussed in reference [1] and recent developments are reviewed in reference [2].

The earliest treatments of band/wheel systems [3–5] focus on the response of a single band span, assuming that the wheels effectively isolate one span from the other. The band is modelled as a straight and tensioned beam translating along its axis with prescribed speed. Analysis of the steady response [3, 4] reveals that the steady beam tension may increase with translation speed to a degree dependent on the wheel support compliance. This tension greatly influences the band natural frequencies, which decrease monotonically with translation speed. For a simply supported beam with finite wheel support compliance, the fundamental natural frequency vanishes at the fundamental *critical speed*, indicating the onset of divergence instability [3–5]. Higher mode divergence and flutter instabilities exist at supercritical speeds.

The above studies consider the *linear* repsonse of a band about the *trivial* (straight) equilibrium. Recent studies [6–9], which consider the geometrically non-linear band response, reveal that the trivial equilibrium undergoes a subcritical pitchfork bifurcation at the first critical speed. This bifurcation generates two non-trivial (buckled) equilibria which remain *stable* for supercritical speeds. Higher order bifurcations occur at each successive critical speed and result in higher order pairs of unstable and non-trivial equilibria [8]. Qualitatively similar behavior has been predicted for simply supported pipes

0022–460X/94/040459 + 25 $08.00/0

conveying high speed fluids [10]. These facts are illustrated in the bifurcation diagram of Figure 1(b), which shows the number and stability of all equilibria that exist for a simply supported beam over a large speed range, see solutions for case $m = 0$. Furthermore, any initial band curvature (induced by bending about supporting wheels) unfolds the fundamental bifurcation, promotes buckling along the path of the "right-branch" equilibrium, and retards the formation of the "left-branch" equilibrium; see solutions for case $m = 4$. Thus, a slightly curved band is expected to gradually and continuously buckle outward as the translation speed is (quasi-statically) increased.

Experiments on band/wheel systems [11] demonstrate that significant vibration coupling exists between upper and lower spans. This coupling between spans, which results from small wheel oscillations, derives from the coupling of longitudinal and transverse band deformations within the individual spans [12, 13]. This latter coupling mechanism results from the initial band curvature. A theoretical model for coupled span response accurately predicts measured free [12] and forced [13] response for subcritical speeds. An alternative model for span-wise coupling is developed in reference [14].

The coupled band/wheel model [12, 13] considers the linear band response about a near-trivial equilibrium. The recent results [6–9] for a (de-coupled) single span, however, suggest that highly non-linear equilibria may also exist for coupled band/wheel systems, particularly at high translation speeds. The objective of this investigation is to examine the general band/wheel system equilibrium and their stability at high translation speeds using both theoretical and experimental methods.

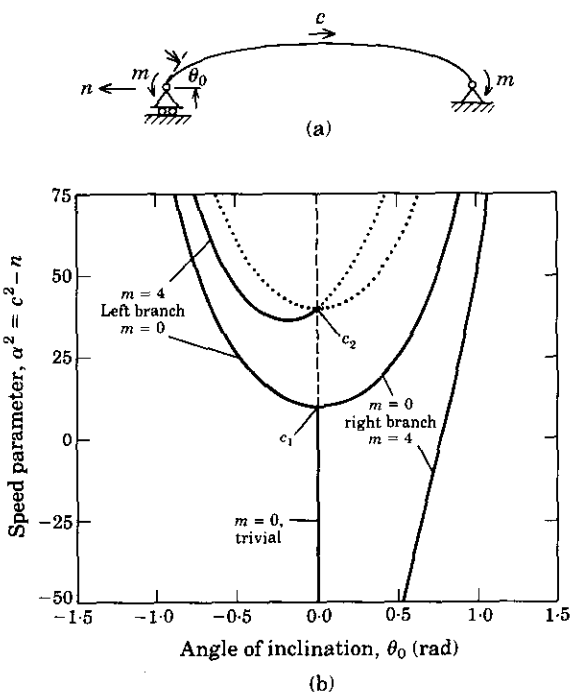

Figure 1. (a) Definition diagram for a single translating beam. (b) Multiple equilibria and solution bifurcations shown in the α^2–θ_0 plane, where α^2 is a measure of the translation speed and θ_0 is a measure of the beam deflection. Stable (——) and unstable (· · ·) equilibria are shown for cases of vanishing ($m = 0$) and significant ($m = 4$) terminal bending moments. In both cases, $n = 100$ and the fundamental and second critical speeds are denoted by c_1 ($\alpha^2 = \pi^2$) and c_2 ($\alpha^2 = 4\pi^2$), respectively.

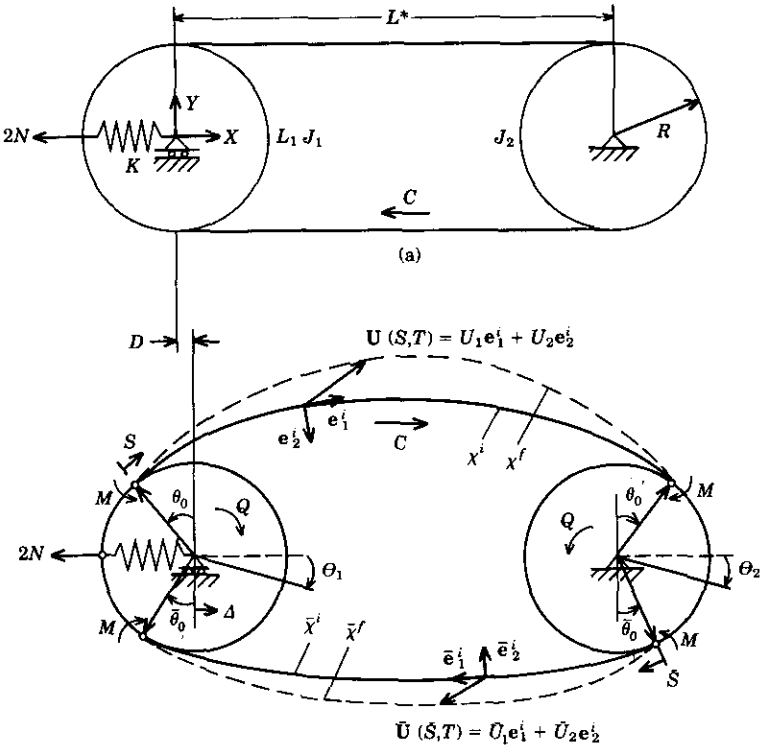

Figure 2. Definition diagram for the band/wheel system. (a) Reference (straight) configuration. (b) Band centerline profile in buckled equilibrium configuration $\chi^i(\bar{\chi}^i)$ (——), and final configuration $\chi^f(\bar{\chi}^f)$ (– – – –). C denotes the band particle translation velocity relative to all profiles.

In this investigation, a theoretical model is derived that describes the planar, non-linear response of a coupled band/wheel system. Elastica theory is used to predict the equilibrium of a continuous band circulating about two wheels. Special attention is paid to determining the location and extent of band/wheel contact and to the effect of steady applied or frictional wheel torques. The equations of motion are linearized about the band equilibrium and local stability is predicted from the eigenvalue problem governing free response. A numerical stability analysis is pursued using a discretized form of the eigenvalue problem. Theoretical predictions of steady and dynamic response are corroborated by results from a companion experimental study.

2. THEORETICAL MODEL

The theoretical model for a single beam developed in reference [8] is presently extended to describe the dynamic response of a continuous band/wheel system. In Figure 2(a) is illustrated a (fictitious) reference configuration in which an inextensible band of length, $2(L^* + \pi R)$, is drawn perfectly straight between two wheels of radius, R, under the action of an infinite load, $N \to \infty$. The band circulates with a steady translation speed, C, in a clockwise direction around the two wheels. The left wheel is elastically restrained in horizontal translation by a spring of stiffness K. For finite and steady N, the left wheel recoils slightly to the right by an amount D, as the band forms the curved equilibrium configuration (solid curves) shown in Figure 2(b). The curve $\chi^i(\bar{\chi}^i)$ denotes the equilibrium

profile of the band centerline for the upper (lower) span which has a free length L ($\bar{L}$) between the points of band/wheel contact. The curvature of $\chi^i(\bar{\chi}^i)$ derives principally from the bending moment M applied at the band/wheel interface. The extreme of the band/wheel contact arc on the upper (lower) span is located by the angle $\theta_0(\bar{\theta}_0)$. The steady torques Q applied at both wheels represent opposing frictional and driving moments which produce a taut lower span and a (relatively) slack upper span.

The planar motion of the upper (lower) span about the equilibrium configuration is described by $\mathbf{U}(S, T)$ ($\bar{\mathbf{U}}(\bar{S}, T)$), where $S(\bar{S})$ denotes the arc length co-ordinate measured along $\chi^i(\bar{\chi}^i)$ and T denotes time. The motion, $\mathbf{U}(S, T) = U_1\mathbf{e}_1^i + U_2\mathbf{e}_2^i$ ($\bar{\mathbf{U}}(\bar{S}, T) = \bar{U}_1\bar{\mathbf{e}}_1^i + \bar{U}_2\bar{\mathbf{e}}_2^i$), describes the final configuration of the centerline profile, $\chi^f(\bar{\chi}^f)$, and is resolved into components aligned with the local tangential direction $\mathbf{e}_1^i$ ($\bar{\mathbf{e}}_1^i$) and the normal direction $\mathbf{e}_2^i$ ($\bar{\mathbf{e}}_2^i$), defined by $\chi^i(\bar{\chi}^i)$. The equations of motion are derived from Hamilton's principle, based on the following assumptions: (1) the beam is a homogeneous, one-dimensional elastic continuum obeying a linear stress–strain relationship; (2) extensions of the beam are described by the Lagrangian strain of the centerline; (3) the motion of the beam is restricted to the X–Y plane; (4) the beam may undergo large static deflections, and additional deflections from the curved equilibrium are described using a non-linear rod theory [15]; (5) rotary inertia due to bending and strain energy due to shear may be neglected assuming that the beam cross-sectional dimensions are small compared to its length; (6) gravitational and dissipative forces may be neglected; (7) the beam mass flux is constant; (8) the influence of the fluid medium (air) may be neglected.

With these assumptions, expressions for strain energy, kinetic energy and work are derived for use in Hamilton's principle. The strain energy of the band in its final configuration is given by [8]

$$\pi_s^f = \pi_s^i + \int_0^L [P^i\Delta\epsilon + \tfrac{1}{2}EA(\Delta\epsilon)^2 + EI\mathscr{K}^i\Delta\mathscr{K} + \tfrac{1}{2}EI(\Delta\mathscr{K})^2]\,\mathrm{d}S + \int_0^{\bar{L}} [\bar{P}^i\Delta\bar{\epsilon} + \tfrac{1}{2}EA(\Delta\bar{\epsilon})^2 + EI\bar{\mathscr{K}}^i\Delta\bar{\mathscr{K}} + \tfrac{1}{2}EI(\Delta\bar{\mathscr{K}})^2]\,\mathrm{d}\bar{S}, \tag{1}$$

where

$$\Delta\epsilon = U_{1,S} - \mathscr{K}^iU_2 + \tfrac{1}{2}[(U_{2,S} + \mathscr{K}^iU_1)^2 + (U_{1,S} - \mathscr{K}^iU_2)^2],$$

$$\Delta\bar{\epsilon} = \bar{U}_{1,S} - \bar{\mathscr{K}}^i\bar{U}_2 + \tfrac{1}{2}[(\bar{U}_{2,S} + \bar{\mathscr{K}}^i\bar{U}_1)^2 + (\bar{U}_{1,S} - \bar{\mathscr{K}}^i\bar{U}_2)^2], \tag{2}$$

$$\Delta\mathscr{K} = a_1a_{2,S}, \qquad \Delta\bar{\mathscr{K}} = \bar{a}_1\bar{a}_{2,S}, \tag{3}$$

$$a_1 = 1 + U_{1,S} - \mathscr{K}^iU_2, \qquad \bar{a}_1 = 1 + \bar{U}_{1,S} - \bar{\mathscr{K}}^i\bar{U}_2, \tag{4}$$

$$a_2 = U_{2,S} + \mathscr{K}^iU_1, \qquad \bar{a}_2 = \bar{U}_{2,S} + \bar{\mathscr{K}}^i\bar{U}_1. \tag{5}$$

In equations (1)–(5), π_s^i is the equilibrium strain energy of the curved bands, $P^i(\bar{P}^i)$ and $\mathscr{K}^i(\bar{\mathscr{K}}^i)$ are the band tension and curvature in $\chi^i(\bar{\chi}^i)$, E is Young's modulus, A is the band cross-sectional area, and I is the principal area moment about the out-of-plane axis through the centroid.

The kinetic energy of the band/wheel system is given by

$$\pi_k^f = \tfrac{1}{2}\rho A\left\{\int_0^L [(U_{1,T} + Ca_1)^2 + (U_{2,T} + Ca_2)^2]\,\mathrm{d}S + \int_0^{\bar{L}} [(\bar{U}_{1,T} + C\bar{a}_1)^2 + (\bar{U}_{2,T} + C\bar{a}_2)^2]\,\mathrm{d}\bar{S}\right\} + \tfrac{1}{2}[J_1(\dot{\Theta}_1)^2 + I_t(\dot{\Delta})^2] + \tfrac{1}{2}J_2(\dot{\Theta}_2)^2, \tag{6}$$

where ρ is the band density, J_1 (J_2) is the moment of inertia of the left (right) wheel about its mass center and I_1 is the mass of the left wheel. The quantities

$$\dot{\Theta}_1 = \frac{\cos\bar{\theta}_0[U_{1,T}(0,T) + Ca_1(0,T)] + \cos\theta_0[\bar{U}_{1,T}(\bar{L},T) + C\bar{a}_1(\bar{L},T)]}{R(\cos\bar{\theta}_0 + \cos\theta_0)},$$

and

$$\dot{\Theta}_2 = [U_{1,T}(L,T) + Ca_1(L,T)]/R$$

represent the angular velocity of the left and right wheel, respectively, and

$$\dot{\Delta} = \frac{[U_{1,T}(0,T) + Ca_1(0,T)] - [\bar{U}_{1,T}(\bar{L},T) + C\bar{a}_1(\bar{L},T)]}{\cos\bar{\theta}_0 + \cos\theta_0}$$

is the (horizontal) velocity of the mass center of the left wheel (see Figure 2(b)).

Additionally, the band displacements at the band/wheel interface must satisfy the following geometric boundary conditions required for vanishing horizontal motion of the right wheel and vanishing vertical motion of both wheels:

$$[U_1(L,T) - \bar{U}_1(0,T)]/(\cos\bar{\theta}_0 + \cos\theta_0) = 0, \tag{7}$$

$$U_2(0,T) = \frac{\sin\theta_0[\bar{U}_1(\bar{L},T) - U_1(0,T)]}{\cos\bar{\theta}_0 + \cos\theta_0}, \quad \text{and} \quad U_2(L,T) = 0, \tag{8}$$

$$U_2(\bar{L},T) = \frac{\sin\bar{\theta}_0[\bar{U}_1(\bar{L},T) - U_1(0,T)]}{\cos\bar{\theta}_0 + \cos\theta_0}, \quad \text{and} \quad \bar{U}_2(0,T) = 0. \tag{9}$$

The virtual work done by the bending moment M, the applied wheel torques Q and the net horizontal force at the left wheel is

$$\delta\pi_w = -M\sigma a_2|_0^L - M\delta\bar{a}_2|_0^{\bar{L}} - [2N + K(\Delta + D)]\delta\Delta + Q\delta\Theta_1 - Q\delta\Theta_2, \tag{10}$$

where D is again the horizontal distance the left wheel moves during the static deformation leading to the equilibrium configuration.

Using equations (1)–(10), Hamilton's principle leads to the following non-linear equations governing planar motion of the band/wheel system:

tangential direction, upper span,

$$[(P^i + AE\Delta\epsilon)a_1]_{,S} - [(P^i + AE\Delta\epsilon)\mathscr{K}^i a_2] + EI[(\mathscr{K}^f a_{2,S})_{,S} + \mathscr{K}^i(K^f a_1)_{,S}]$$
$$= \rho A[U_{1,TT} + 2Ca_{1,T} + C^2(a_{1,S} - \mathscr{K}^i a_2)]; \tag{11}$$

tangential direction, lower span,

$$[(\bar{P}^i + AE\Delta\bar{\epsilon})\bar{a}_1]_{,\bar{S}} - [(\bar{P}^i + AE\Delta\bar{\epsilon})\bar{\mathscr{K}}^i\bar{a}_2] + EI[(\bar{\mathscr{K}}^f\bar{a}_{2,\bar{S}})_{,\bar{S}} + \bar{\mathscr{K}}^i(\bar{K}^f\bar{a}_1)_{,\bar{S}}]$$
$$= \rho A[\bar{U}_{1,TT} + 2C\bar{a}_{1,T} + C^2(\bar{a}_{1,\bar{S}} - \bar{\mathscr{K}}^i\bar{a}_2)]; \tag{12}$$

normal direction, upper span,

$$[(P^i + AE\Delta\epsilon)a_2]_{,S} + \mathscr{K}^i a_1[P^i + AE\Delta\epsilon] + EI[\mathscr{K}^f\mathscr{K}^i a_{2,S} - (\mathscr{K}^f a_1)_{,SS}]$$
$$= \rho A[U_{2,TT} + 2Ca_{2,T} + C^2(a_{2,S} + \mathscr{K}^i a_1)]; \tag{13}$$

normal direction, lower span,

$$[(\bar{P}^i + AE\Delta\bar{\epsilon})\bar{a}_2]_{,\bar{S}} + \bar{\mathscr{K}}^i\bar{a}_1[\bar{P}^i + AE\Delta\bar{\epsilon}] + EI[\bar{\mathscr{K}}^f\bar{\mathscr{K}}^i\bar{a}_{2,\bar{S}} - (\bar{\mathscr{K}}^f\bar{a}_1)_{,\bar{S}\bar{S}}]$$
$$= \rho A[\bar{U}_{2,TT} + 2C\bar{a}_{2,T} + C^2(\bar{a}_{2,\bar{S}} + \bar{\mathscr{K}}^i\bar{a}_1)]; \tag{14}$$

with the natural boundary conditions

$$I_1\Delta_{,TT}+\rho AC\{\cos\bar{\theta}_0[\bar{U}_{1,T}(\bar{L},T)+C\bar{a}_1(\bar{L},T)]+\sin\bar{\theta}_0[\bar{U}_{2,T}(\bar{L},T)+C\bar{a}_2(\bar{L},T)]$$
$$+\cos\theta_0[U_{1,T}(0,T)+Ca_1(0,T)]-\sin\theta_0[U_{2,T}(0,T)+Ca_2(0,T)]\}$$
$$+EI[\bar{\mathscr{K}}^f(\bar{L},T)\sin\bar{\theta}_0-\mathscr{K}^f(0,T)\sin\theta_0]-\cos\bar{\theta}_0[\bar{P}^i(\bar{L})+EA\Delta\bar{\epsilon}(\bar{L},T)]$$
$$-\cos\theta_0[P^i(0)+EA\Delta\epsilon(0,T)]+2N+K(\Delta+D)=0, \tag{15}$$

$$\frac{J_1\Theta_{1,TT}}{R}-\rho AC\{[\bar{U}_{1,T}(\bar{L},T)+C\bar{a}_1(\bar{L},T)]-[U_{1,T}(0,T)+Ca_1(0,T)]\}$$
$$-[\bar{P}^i(\bar{L})+EA\Delta\bar{\epsilon}(\bar{L},T)]-P^i(0)+EA\Delta\epsilon(0,T)]-T/R=0, \tag{16}$$

$$\frac{J_2}{R}\Theta_{2,TT}+\rho AC\{[\bar{U}_{1,T}(0,T)+C\bar{a}_1(0,T)]-[U_{1,T}(L,T)+Ca_1(L,T)]\}$$
$$+P^i(L)-\bar{P}^i(0)+EA[\Delta\epsilon(L,T)-\Delta\bar{\epsilon}(0,T)]+T/R=0, \tag{17}$$

$$EI\mathscr{K}^f a_1+M=0, \qquad \text{at } S=0,L, \tag{18}$$

$$EI\bar{\mathscr{K}}^f\bar{a}_1+M=0, \qquad \text{at } \bar{S}=0,\bar{L}, \tag{19}$$

and geometric boundary conditions (7)–(9).

For convenience in the subsequent analysis, the following non-dimensional variables are introduced:

$$s=S/L^*, \quad \bar{s}=\bar{S}/L^*, \quad \kappa=L^*\mathscr{K}^i, \quad \bar{\kappa}=L^*\bar{\mathscr{K}}^i,$$
$$d=D/L^*, \quad r=R/L^*, \quad l=L/L^*,$$
$$\bar{l}=\bar{L}/L^*, \quad n=N(L^*)^2/EI, \quad m=ML^*/EI, \quad k=K(L^*)^3/EI,$$
$$q=QL^*/EI, \quad x=X/L^*, \quad y=Y/L^*,$$
$$\gamma=A(L^*)^2/I, \quad c^2=\rho A(L^*C)^2/EI, \quad p=P^i(L^*)^2/EI,$$
$$\bar{p}=\bar{P}^i(L^*)^2/EI, \quad t=T\sqrt{EI/[\rho A(L^*)^4]},$$
$$u_1=U_1/L^*, \quad \bar{u}_1=\bar{U}_1/L^*, \quad u_2=U_2/L^*, \quad \bar{u}_2=\bar{U}_2/L^*,$$
$$i_1=I_1/\rho AL^*, \quad j_1=J_1/[\rho A(L^*)^3], \quad j_2=J_2/[\rho A(L^*)^3].$$

3. EQUILIBRIUM ANALYSIS

The equilibrium of an axially moving beam was partially analyzed by Chubachi [3], whose linear analysis was used to predict the critical speeds of a simply supported beam. Extensions of this equilibrium problem, which consider geometrically non-linear beam deflections, have been analyzed recently using closed form [6, 8] and approximate [9] solution methods (refer to Figure 1). All models used consider a *single* beam of *fixed length* (L) which approximates the response of one span in a band/wheel system. For steady response, this approximation remains valid, provided that the lateral band deflections do not significantly alter the free span lengths and the band/wheel contact points. Thus, for small deflections of a highly tensioned band, the points of band/wheel contact are approximately, diametrically opposite (i.e., $\theta_0\approx\bar{\theta}_0\approx 0$), and the free span length ($L\approx\bar{L}$) can be prescribed as in previous models for band/wheel systems [11–14]. The present model offers a more complete description by considering *geometrically large deflections* of a continuous band wrapped about two wheels. For large deflections, the free span lengths

$(L, \bar{L})$ and the location of the band/wheel contact points $(\theta_0, \bar{\theta}_0)$ are not known *a priori*. Instead, they must be determined from the equilibrium conditions governing the steady response of the entire band/wheel system.

The equations of equilibrium are extracted from the response model equations (7)–(9) and equations (11)–(19) by equating the dynamic displacement components U_1, $\bar{U}_1$, U_2 and $\bar{U}_2$ to zero. This procedure provides the following non-linear boundary value problem for solution of the (non-dimensional) equilibrium band curvatures $\kappa(s)$, $\bar{\kappa}(\bar{s})$ and tensions $p(s)$, $\bar{p}(\bar{s})$:

$$p' + \kappa\kappa' = 0, \qquad 0 < s < l, \tag{20}$$

$$\kappa'' + (c^2 - p)\kappa = 0, \qquad 0 < s < l, \tag{21}$$

$$\bar{p}' + \bar{\kappa}\kappa' = 0, \qquad 0 < \bar{s} < \bar{l}, \tag{22}$$

$$\kappa'' + (c^2 - \bar{p})\bar{\kappa} = 0, \qquad 0 < \bar{s} < \bar{l}, \tag{23}$$

with the boundary conditions

$$\kappa(0) = \kappa(l) = -m, \qquad \bar{\kappa}(0) = \bar{\kappa}(\bar{l}) = -m, \tag{24, 25}$$

$$p(0)\cos\theta_0 + \bar{p}(\bar{l})\cos\theta_0 - \kappa'(0)\sin\theta_0 + \bar{\kappa}'(\bar{l})\sin\bar{\theta}_0 = 2n + kd + c^2(\cos\theta_0 + \cos\bar{\theta}_0), \tag{26}$$

$$r[\bar{p}(\bar{l}) - p(0)] = q. \tag{27}$$

The boundary conditions (26) and (27) describe horizontal force and moment equilibrium of the left wheel, respectively. These two boundary conditions and the inextensibility constraint,

$$l + \bar{l} + 2r(\pi - \theta_0 - \bar{\theta}_0) = 2(1 + \pi r), \tag{28}$$

couple the static deflections of the upper span to those of the lower span.

Closed form solutions of equations (20)–(28) are obtained in terms of elliptic integrals as follows. Integrating equations (20) and (22) and substituting the results into equations (21) and (23), respectively, leads to

$$\kappa'' + (c^2 - \beta + \tfrac{1}{2}\kappa^2)\kappa = 0, \qquad 0 < s < l, \tag{29}$$

$$\bar{\kappa}'' + (c^2 - \bar{\beta} + \tfrac{1}{2}\bar{\kappa}^2)\bar{\kappa} = 0, \qquad 0 < \bar{s} < \bar{l}, \tag{30}$$

subject to boundary conditions (24) and (25). The constants β and $\bar{\beta}$ are first integrals of equations (20) and (22), given by

$$\beta = p(s) + \tfrac{1}{2}\kappa^2(s) = \frac{(2n + kd)\cos\theta_0\cos\bar{\theta}_0}{\cos\theta_0 + \cos\bar{\theta}_0} + c^2 - \frac{q\cos\theta_0}{r(\cos\theta_0 + \cos\bar{\theta}_0)} + \tfrac{1}{2}m^2, \tag{31}$$

$$\bar{\beta} = \bar{p}(\bar{s}) + \tfrac{1}{2}\bar{\kappa}^2(\bar{s}) = \frac{(2n + kd)\cos\theta_0\cos\bar{\theta}_0}{\cos\theta_0 + \cos\bar{\theta}_0} + c^2 + \frac{q\cos\bar{\theta}_0}{r(\cos\theta_0 + \cos\bar{\theta}_0)} + \tfrac{1}{2}m^2, \tag{32}$$

and were evaluated using equations (24)–(27). Let $\theta(s)$ $(\bar{\theta}(\bar{s}))$ denote the angle of inclination of the equilibrium tangent $\mathbf{e}_1^i$ $(\bar{\mathbf{e}}_1^i)$ above (below) the horizontal. Then the (terminal contact) angles $\theta_0 = \theta(0)$ and $\bar{\theta}_0 = \bar{\theta}(0)$ and the free span lengths l and $\bar{l}$ depend on the equilibrium curvatures $\kappa(s) = \theta'(s)$ and $\bar{\kappa}(\bar{s}) = \bar{\theta}'(\bar{s})$ through the static displacement of the left wheel

$$d = l + 2r(\sin\theta_0 - \theta_0) - \int_0^l \cos\theta(s)\,\mathrm{d}s, \qquad d = \bar{l} + 2r(\sin\bar{\theta}_0 - \bar{\theta}_0) - \int_0^{\bar{l}} \cos\bar{\theta}(\bar{s})\,\mathrm{d}\bar{s}, \tag{33, 34}$$

and the inextensibility constraint (28). In addition, the constraints $\kappa'(0)$, $\kappa'(l) > 0$ and $\bar{\kappa}'(0)$, $\bar{\kappa}'(\bar{l}) > 0$ must also be imposed to ensure that the equilibrium band solution does not penetrate the wheels.

Note from equations (31) and (32) that $c^2 - \beta$ and $c^2 - \bar{\beta}$ are dependent of c and, thus, the entire boundary value problem governing the equilibrium geometry (29) and (30) with equations (24), (25), (28) and (31)–(34) is *independent* of the translation speed c. By contrast, the equilibrium boundary value problem for the single axially moving beam model is translation speed dependent [8] due to the change in character of the horizontal force balance boundary condition (26) [16].

In this study, attention is focused on the equilibrium solution which resembles the fundamental buckling mode of a simply supported beam. This solution is symmetric about the mid-spans, $s^* = l/2$ and $\bar{s}^* = \bar{l}/2$. Following the procedure in reference [8], the curvature extrema $\kappa(s^*)$ and $\bar{\kappa}(\bar{s}^*)$ are given by

$$\kappa(s^*) = -\left\{4\sin^2\frac{\theta_0}{2}\left[-\frac{2n+kd}{\cos\theta_0+\cos\bar{\theta}_0}\cos\bar{\theta}_0+\frac{q}{r(\cos\theta_0+\cos\bar{\theta}_0)}\right]+m^2\right\}^{1/2}, \tag{35}$$

$$\bar{\kappa}(\bar{s}^*) = -\left\{4\sin^2\frac{\bar{\theta}_0}{2}\left[-\frac{2n+kd}{\cos\theta_0+\cos\bar{\theta}_0}\cos\theta_0-\frac{q}{r(\cos\theta_0+\cos\bar{\theta}_0)}\right]+m^2\right\}^{1/2}, \tag{36}$$

and are used in the change of variables leading to elliptic integral solutions to equations (29) and (30). Using the change of variables

$$\eta = \cos^{-1}\left[\frac{\kappa^2(s)-\kappa^2(s^*)}{4(\beta-c^2)-2\kappa^2(s^*)}\right]^{1/2}$$

in equation (29), and

$$\bar{\eta} = \cos^{-1}\left[\frac{\bar{\kappa}^2(\bar{s})-\bar{\kappa}^2(\bar{s}^*)}{4(\bar{\beta}-c^2)-2\bar{\kappa}^2(\bar{s}^*)}\right]^{1/2}$$

in equation (30), and integrating, provides general solutions for $\kappa(s)$ and $\bar{\kappa}(\bar{s})$ in terms of incomplete elliptic integrals of the first kind:

$$l/2 - s = \xi\int_{\phi(s)}^{\pi/2}\frac{d\eta}{\sqrt{1-\mu^2\sin^2\eta}}, \qquad 0 \leqslant s \leqslant s^* = l/2, \tag{37}$$

$$\bar{l}/2 - \bar{s} = \bar{\xi}\int_{\bar{\phi}(\bar{s})}^{\pi/2}\frac{d\bar{\eta}}{\sqrt{1-\bar{\mu}^2\sin^2\bar{\eta}}}, \qquad 0 \leqslant \bar{s} \leqslant \bar{s}^* = \bar{l}/2, \tag{38}$$

where

$$\xi = \frac{2}{\sqrt{4(\beta-c^2)-\kappa^2(s^*)}}, \qquad \bar{\xi} = \frac{2}{\sqrt{4(\bar{\beta}-c^2)-\bar{\kappa}^2(\bar{s}^*)}}, \tag{39}$$

$$\mu^2 = \frac{4(\beta-c^2)-2\kappa^2(s^*)}{4(\beta-c^2)-\kappa^2(s^*)}, \qquad \bar{\mu}^2 = \frac{4(\bar{\beta}-c^2)-2\bar{\kappa}^2(\bar{s}^*)}{4(\bar{\beta}-c^2)-\bar{\kappa}^2(\bar{s}^*)}, \tag{40}$$

$$\phi(s) = \cos^{-1}\left[\frac{\kappa^2(s)-\kappa^2(s^*)}{4(\beta-c^2)-2\kappa^2(s^*)}\right]^{1/2}, \qquad \bar{\phi}(\bar{s}) = \cos^{-1}\left[\frac{\bar{\kappa}^2(\bar{s})-\bar{\kappa}^2(\bar{s}^*)}{4(\bar{\beta}-c^2)-2\bar{\kappa}^2(\bar{s}^*)}\right]^{1/2}. \tag{41}$$

The general solutions, equations (37) and (38), contain the five unknown constants θ_0, $\bar{\theta}_0$, l, $\bar{l}$ and d, which must be selected to satisfy the two boundary conditions $\kappa(0) = -m$, $\bar{\kappa}(0) = -m$, and the three constraint equations (28), (33) and (34). (The remaining two boundary conditions $\kappa(l) = -m$ and $\bar{\kappa}(\bar{l}) = -m$ are satisfied by solution symmetry.) Application of these boundary conditions in equations (37) and (38) and substitution into

equations (28), (33) and (34) leads to three non-linear equations in the three unknowns θ_0, $\bar{\theta}_0$ and d:

$$\xi \int_{\phi(0)}^{\pi/2} \frac{d\eta}{\sqrt{1-\mu^2 \sin^2 \eta}} + \bar{\xi} \int_{\bar{\phi}(0)}^{\pi/2} \frac{d\bar{\eta}}{\sqrt{1-\bar{\mu}^2 \sin^2 \bar{\eta}}} = 1 + r(\theta_0 + \bar{\theta}_0), \tag{42}$$

$$(1-d)/2 + r \sin \theta_0 = \xi \int_{\phi(0)}^{\pi/2} \frac{(1-2\sin^2 \eta)\, d\eta}{\sqrt{1-\mu^2 \sin^2 \eta}}, \tag{43}$$

$$(1-d)/2 + r \sin \bar{\theta}_0 = \bar{\xi} \int_{\bar{\phi}(0)}^{\pi/2} \frac{(1-2\sin^2 \bar{\eta})\, d\bar{\eta}}{\sqrt{1-\bar{\mu}^2 \sin^2 \bar{\eta}}}. \tag{44}$$

The constants θ_0, $\bar{\theta}_0$ and d are then determined by simultaneous (numerical) solution of equations (42)–(44), and $\bar{l}$ and l are determined by evaluating equation (37) at $s = 0$ and equation (38) at $\bar{s} = 0$, respectively. The example solutions below were obtained from equations (42)–(44), using Newton–Raphson iteration.

3.1. EXAMPLE EQUILIBRIUM SOLUTIONS

A first example is considered for which $k = 0$, $m = 4$ ($r = \frac{1}{4}$) and $q = 0$. This example, referred to herein as the "baseline case", describes a symmetric ($q = 0$), free-center ($k = 0$) band/wheel system where the wheel radius R is one-quarter of the reference free span length L^* ($r = \frac{1}{4}$ and $m = 4$). The computed equilibrium solution in the $\theta_0 (= \bar{\theta}_0)$–$n$ and d–n planes is illustrated in Figure 3. As the static load increases slowly (quasi-statically), both the contact angles θ_0 and $\bar{\theta}_0$ and the wheel displacement d approach zero (refer to Figure 2(a)). As the static load decreases slowly from $n = 80$, the band buckles further away from the trivial reference configuration ($\theta_0 = \bar{\theta}_0$ increase) in a smooth and monotone fashion. The band/wheel model assumed ideal (no-slip) band/wheel contact and the contact angles θ_0 and $\bar{\theta}_0$ would approach the limiting value $\theta_0 = \bar{\theta}_0 \to \pi/2$ for a vanishing contact arc in the limit $n \to 0$. In actual band/wheel systems, the band would lose traction before this limit, and the current model could no longer apply.

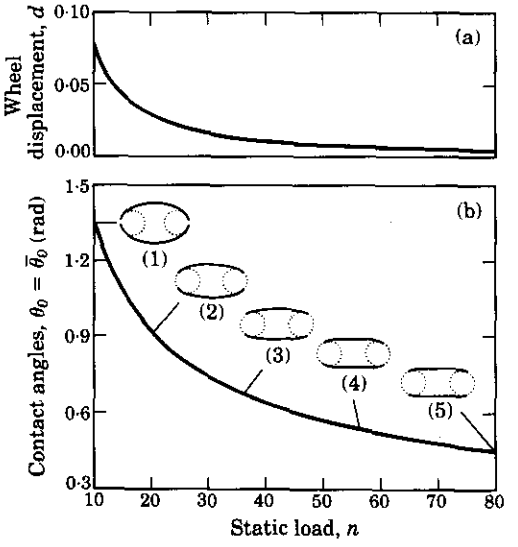

Figure 3. Equilibrium solutions for the baseline case ($k = 0, m = 4, r = \frac{1}{4}$ and $q = 0$) in (a) the d–n plane and (b) the $\theta_0 (= \bar{\theta}_0)$–$n$ plane. Equilibria are shown for: (1) $n = 10$; (2) $n = 20{\cdot}25$; (3) $n = 36$; (4) $n = 56{\cdot}25$; (5) $n = 80$. (——), Free span length; · · · ·, wheels.

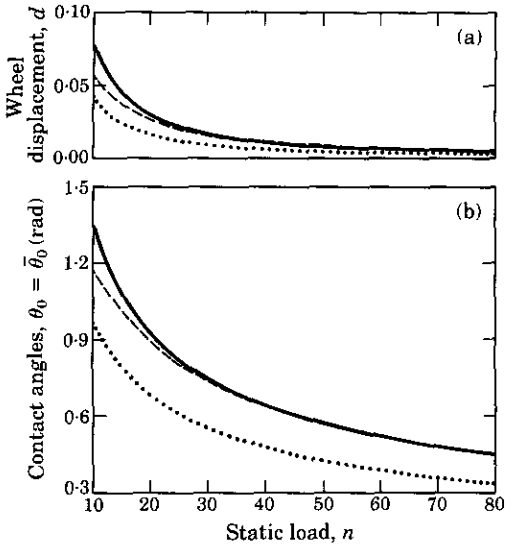

Figure 4. The sensitivity of the equilibrium solution to support stiffness and wheel radius. Results shown in the (a) d–n plane and (b) $\theta_0(=\bar{\theta}_0)$–$n$ plane. Three cases are considered: $k = 0$, $m = 4$ (——); $k = 100$, $m = 4$ (– – – –); $k = 0$, $m = 3$ (· · · · ·). In all cases, $q = 0$.

Representative band/wheel equilibrium configurations are shown in Figure 3 for five values of the static load n. The equilibrium configuration is readily obtained from the determined equilibrium curvature solutions $\kappa(s) = \theta'(s)$ and $\bar{\kappa}(\bar{s}) = \bar{\theta}'(s)$, using

$$x(s) = \int_0^s \cos\theta(\eta)\,d\eta + d + r(1 - \sin\theta_0), \qquad y(s) = \int_0^s \sin\theta(\eta)\,d\eta + r\cos\theta_0,$$

$$\bar{x}(\bar{s}) = -\int_0^{\bar{s}} \cos\bar{\theta}(\eta)\,d\eta + \bar{l} + r(1 + \sin\theta_0), \qquad \bar{y}(\bar{s}) = -\int_0^{\bar{s}} \sin\bar{\theta}(\eta)\,d\eta + r\cos\theta_0.$$

An evolution of band/wheel equilibria is illustrated in Figure 3(b) by the sequence numbered (1) to (5). The solid curves represent the free span lengths and the dotted curves represent the wheel perimeters. In the absence of any wheel torque q, the two spans are equally tensioned and are symmetric images about the x-axis. As the static load decreases from $n = 80$, the band buckles away from this line of symmetry and partially unwraps from the wheels, while the left wheel recoils slightly to the right. Consequently, the free span lengths *increase* with decreasing static load as the band/wheel contact points slowly migrate towards their limiting position $\theta_0 = \bar{\theta}_0 \to \pi/2$.

The sensitivity of the equilibrium to changes in either support stiffness or wheel radius (bending moment) is illustrated in Figure 4. The previous solutions for the baseline case ($k = 0, m = 4$) are reproduced in Figure 4, where they are compared with those of two other band/wheel systems described by (1) non-zero support stiffness ($k = 100, m = 4$), and (2) reduced bending moment ($k = 0, m = 3$). The comparison reveals that, as expected, either increasing the support stiffness or reducing the bending moment reduces the magnitudes of the wheel and band displacements for a given static load.

The addition of steady wheel torques q breaks the system symmetry and leads to a taut lower span and a (relatively) slack upper span. This conclusion is apparent in Figure 5, which compares the baseline case ($q = 0$) to the case of a small wheel torque $q = 2$. In the latter case, $\bar{\theta}_0 < \theta_0$, and the free length of the (slack) upper span slightly exceeds that of the lower span; see the illustrated equilibrium configuration for case $n = 16$. Note again

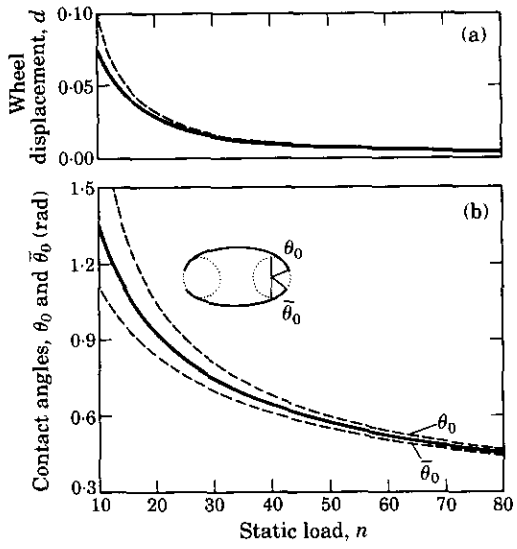

Figure 5. Sensitivity of the equilibrium solution to small steady wheel torques. Results shown in (a) the d–n plane and (b) the θ_0, $\bar{\theta}_0$–n plane. Two cases are considered: $q = 0$ (——, $\theta_0 = \bar{\theta}_0$) and $q = 2$ (– – –, $\theta_0 > \bar{\theta}_0$). In both cases, $k = 0$ and $m = 4$. The equilibrium configuration is shown for the case $n = 16$.

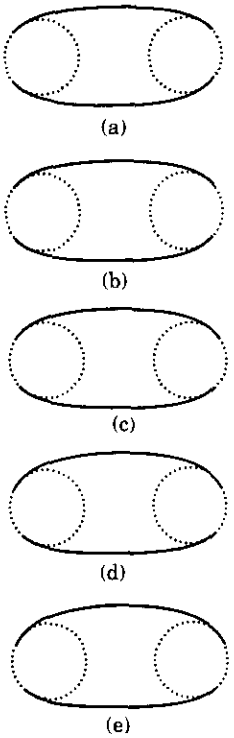

Figure 6. Torque-induced asymmetry. The equilibrium configuration is shown for five values of steady torque: (a) $q = 0$; (b) $q = 1$; (c) $q = 2$; (d) $q = 4$; (e) $q = 5$. In all cases, $k = 0$, $m = 4$ and $n = 23{\cdot}4$.

that the contact arc would ultimately vanish with decreasing static load; that is, $|\theta_0| + |\bar{\theta}_0| \to \pi$ as $n \to 0$. The gradual distortion of the symmetric equilibrium configuration ($q = 0$) under increasing torque values is illustrated in Figure 6. For the five cases shown, the static load is kept constant ($n = 23{\cdot}4$) while the torque is slowly (quasi-statically) increased. The asymmetry induced by the applied torque is clearly visible for the larger torque values considered in cases (d), $q = 4$, and (e), $q = 5$.

The above examples illustrate how the equilibrium geometry of the band/wheel system depends on the steady applied load, n, the wheel radius of curvature, ($r = 1/m$), the support stiffness k, and the steady wheel torques q. These results are not affected by the band translation speed c, since, as shown above, the boundary value problem for the equilibrium curvature is independent of c. However, the translation speed does affect the equilibrium tension. As seen from equations (31) and (32), the equilibrium span tension $p(s)$ and $\bar{p}(s)$ increase as the square of the translation speed. A similar result is obtained in references [3, 4], where the degree of speed tensioning is controlled by the support compliance. The result of references [3, 4], however, follows from considering the *linear extension of a perfectly straight band.* The present results (31) and (32) follow from considering the *non-linear inextensible deformation of a curved band.* In the case of a buckled band with a compliant support, the additional deformation due to band extension is negligible [17].

4. ANALYSIS OF FREE LINEAR RESPONSE

To investigate the local stability of the equilibria, the non-linear equations of planar motion (11)–(14) are linearized about an arbitrary equilibrium that is described by its curvature κ ($\bar{\kappa}$) and tension p ($\bar{p}$). The linearized (non-dimensional) equations governing free, planar response are as follows:

tangential direction, upper span,

$$[(\gamma + p - c^2)(u_{1,s} - \kappa u_2)]_{,s} + [\kappa(c^2 - p)][u_{2,s} + \kappa u_1] + \kappa[u_{2,s} + \kappa u_1]_{,ss} + [\kappa a_{2,s}]_{,s} + \kappa\kappa_{,s}(a_1 - 1) + \kappa^2 a_{1,s} = u_{1,tt} + 2c[u_{1,s} - \kappa u_2]_{,t}; \tag{45}$$

tangential direction, lower span,

$$[(\gamma + \bar{p} - c^2)(\bar{u}_{1,\bar{s}} - \bar{\kappa}\bar{u}_2)]_{,\bar{s}} + [\bar{\kappa}(c^2 - \bar{p})][\bar{u}_{2,\bar{s}} + \bar{\kappa}\bar{u}_1] + \bar{\kappa}[\bar{u}_{2,\bar{s}} + \bar{\kappa}\bar{u}_1]_{,\bar{s}\bar{s}} + [\bar{\kappa}\bar{a}_{2,\bar{s}}]_{,\bar{s}} + \bar{\kappa}\bar{\kappa}_{,\bar{s}}(\bar{a}_1 - 1) + \bar{\kappa}^2\bar{a}_{1,\bar{s}} = \bar{u}_{1,tt} + 2c[\bar{u}_{1,\bar{s}} - \bar{\kappa}\bar{u}_2]_{,t}; \tag{46}$$

normal direction, upper span,

$$[\kappa(\gamma + p - c^2)][u_{1,s} - \kappa u_2] + [(p - c^2)(u_{2,s} + \kappa u_1)]_{,s} - [u_{2,s} + \kappa u_1]_{,sss} - [\kappa(a_1 - 1)]_{,ss} + \kappa^2 a_{2,s} = u_{2,tt} + 2c[u_{2,s} + \kappa u_1]_{,t}; \tag{47}$$

normal direction, lower span,

$$[\bar{\kappa}(\gamma + \bar{p} - c^2)][\bar{u}_{1,\bar{s}} - \bar{\kappa}\bar{u}_2] + [(\bar{p} - c^2)(\bar{u}_{2,\bar{s}} + \bar{\kappa}\bar{u}_1)]_{,\bar{s}} - [\bar{u}_{2,\bar{s}} + \bar{\kappa}\bar{u}_1]_{,\bar{s}\bar{s}\bar{s}} - [\bar{\kappa}(\bar{a}_1 - 1)]_{,\bar{s}\bar{s}} + \bar{\kappa}^2\bar{a}_{2,\bar{s}} = \bar{u}_{2,tt} + 2c[\bar{u}_{2,\bar{s}} + \bar{\kappa}\bar{u}_1]_{,t}. \tag{48}$$

The linearized boundary conditions are extracted from the boundary conditions (7)–(9)

and (15)–(19), after incorporating the boundary conditions for the equilibrium equations, (24)–(27). The linearized boundary conditions are:

$$i_1\zeta_{,tt} + c[\cos\bar{\theta}\bar{u}_{1,s}(\bar{l},t) + \cos\theta u_{1,s}(0,t)] + (c^2-1)$$
$$\times\{\cos\bar{\theta}[\bar{a}_1(\bar{l},t)-1] + \cos\theta[a_1(0,t)-1]\}$$
$$-\sin\theta\{c[u_{2,t}(0,t) + ca_2(0,t)] + a_{2,ss}(0,t)\}$$
$$+\sin\bar{\theta}\{c[\bar{u}_{2,t}(\bar{l},t) + c\bar{a}_2(\bar{l},t)] + \bar{a}_{2,\bar{s}\bar{s}}(\bar{l},t)\} + \kappa\zeta = 0, \tag{49}$$

$$j_1\Theta_{1,tt}/r + c[u_{1,t}(0,t) - \bar{u}_{1,t}(\bar{l},t)] + (c^2-1)$$
$$\times[u_{1,s}(0,t) - \kappa(0)u_2(0,t) - \bar{u}_{1,\bar{s}}(\bar{l},t) + \bar{\kappa}(\bar{l})\bar{u}_2(\bar{l},t)] = 0, \tag{50}$$

$$j_2\Theta_{2,tt}/r + c[\bar{u}_{1,t}(0,t) - u_{1,t}(l,t)] + (c^2-1)$$
$$\times[\bar{u}_{1,\bar{s}}(0,t) - \bar{\kappa}(0)\bar{u}_2(0,t) - u_{1,s}(l,t) + \kappa(l)u_2(l,t)] = 0, \tag{51}$$

$$(u_{2,s} + \kappa u_1)_{,s}|_0^l = 0, \qquad (\bar{u}_{2,\bar{s}} + \bar{\kappa}\bar{u}_1)_{,s}|_0^{\bar{l}} = 0, \tag{52, 53}$$

$$u_1(l,t) = \bar{u}_1(0,t), \qquad u_2(l,t) = \bar{u}_2(0,t) = 0, \tag{54, 55}$$

$$u_2(0,t) = \frac{\sin\theta_0}{\cos\theta_0 + \cos\bar{\theta}}[\bar{u}_1(\bar{l},t) - u_1(0,t)], \qquad \bar{u}_2(\bar{l},t) = \frac{\sin\bar{\theta}_0}{\cos\theta_0 + \cos\bar{\theta}}[\bar{u}_1(\bar{l},t) - u_1(0,t)], \tag{56, 57}$$

where $\zeta(t) = \Delta(t)/L^*$ is the (non-dimensional) translation of the left wheel.

Motion about a specific equilibrum is examined by prescribing the equilibrium curvature κ ($\bar{\kappa}$) and tension p ($\bar{p}$), which appear as (non-constant) coefficients in equations (45)–(48). Exact expressions for κ ($\bar{\kappa}$), in terms of elliptic integrals, are obtained from equations (37)–(44). The equilibrium tension follows from the solution for κ ($\bar{\kappa}$) by evaluating equations (31) and (32).

4.1. NUMERICAL ANALYSIS

A numerical method is adopted to compute the free response about the band/wheel system equilibrium. The Ritz method is used to discretize the linear equations of motion, and vibration and stability characteristics are determined from the eigensolutions of the discrete model.

Consider the H-term representations for u_1, $\bar{u}_1$, u_2 and $\bar{u}_2$ of the form

$$u_1(s,t) = \sum_{j=0}^{H}\phi_{1j}(t)\Phi_{1j}(s), \qquad \bar{u}_1(\bar{s},t) = \sum_{j=0}^{H}\phi_{2j}(t)\Phi_{2j}(\bar{s}), \tag{58, 59}$$

$$u_2(s,t) = \sum_{j=1}^{H}\phi_{3j}(t)\Phi_{3j}(s), \qquad \bar{u}_2(\bar{s},t) = \sum_{j=1}^{H}\phi_{4j}(t)\Phi_{4j}(\bar{s}), \tag{60, 61}$$

where $\Phi_{1j}(s) = \cos(j\pi s/l)$, $\Phi_{2j}(\bar{s}) = \cos(j\pi\bar{s}/\bar{l})$, $\Phi_{3j}(s) = \sin(j\pi s/l) + \cos((2j-1)\pi s/2l)$ and $\Phi_{4j}(\bar{s}) = \sin(j\pi(\bar{l}-\bar{s})/\bar{l}) + \cos((2j-1)\pi(\bar{l}-\bar{s})/2\bar{l}$. Note that Φ_{1j}, Φ_{2j}, Φ_{3j} and Φ_{4j} are almost admissible functions which satisfy, *a priori*, the geometric boundary conditions (55). Note also that $\Phi_{1j} = \Phi_{2j}$, $j = 0, 1, \ldots$, are the eigenfunctions for a free–free rod and include the *rod* rigid body mode ($j = 0$). Substitution of equations (58)–(61) into Hamilton's principle (retaining quadratic energy terms only) and elimination of three co-ordinates using the three remaining geometric boundary conditions (54), (56) and (57), provides a set of $4H - 1$ coupled, ordinary differential equations for solution of $4H - 1$ generalized co-ordinates $\phi_{ij}(t)$:

$$\mathbf{M}\ddot{\vec{\phi}} + \mathbf{G}\dot{\vec{\phi}} + \mathbf{K}\vec{\phi} = \vec{0}. \tag{62}$$

The elements of the matrices **M**, **G** and **K**, which are given in reference [16], are evaluated by numerical quadrature. These matrices depend on the equilibrium state under consideration and are evaluated using the elliptic integral solutions for κ ($\bar{\kappa}$) and p ($\bar{p}$), given in section 3. The matrices **M** and **K** are symmetric, while **G** is skew symmetric and proportional to the translation speed c. Furthermore, **M** is positive definite while **K** is, in general, sign indefinite.

Using $\vec{\phi}(t) = \vec{Q}\,e^{\omega t}$ in equation (62) leads to the discrete eigenvalue problem governing free response

$$[\omega^2\mathbf{M} + \omega\mathbf{G} + \mathbf{K}]\vec{Q} = \vec{0}. \tag{63}$$

The natural frequencies and mode shapes for the band/wheel model are obtained numerically from equation (63). In this discrete formulation, the natural frequencies of the translating band/wheel model are given by the imaginary parts of the eigenvalues, $\mathrm{Im}\,[\omega_l]$, $l = 1, 2, \ldots, 4H - 1$, and the eigenfunctions are obtained from the eigenvectors $\vec{Q}_l$, $l = 1, 2, \ldots, 4H - 1$, through equations (58)–(61). In general, these eigensolutions are complex.

4.2. COMPARISON WITH PREVIOUS BAND/WHEEL MODEL

An important comparison is made with the previous band/wheel model of Wang and Mote [12, 13]. Four qualitative differences distinguish the current model from that used in reference [12, 13]. First, the current model considers large static band deflections and therefore include the possibilities that (1) the points of band/wheel contact may not be diameterically opposite ($\theta_0 \neq 0, \bar{\theta}_0 \neq 0$), and (2) the free span lengths are not necessarily equal to the center-to-center distance between the wheels ($l \neq 1, \bar{l} \neq 1$). These considerations lead to a more complex coupling between the upper and lower spans, as shown by the boundary conditions (49)–(51) and (56)–(57). These boundary conditions reduce to those used in references [12, 13] for the special case $\theta_0 = \bar{\theta}_0 = 0$ and $l = \bar{l} = 1$. Second, the large static band deflections considered herein are described using inextensible elastica theory. This is in contrast with the model of references [12, 13] which considers relatively small, but *extensible*, static band deformations. As a result, the equilibrium curvature provides the speed-tensioning mechanism in the current model, while small band extensions provide this effect in the model of reference [12, 13] (refer to discussion in section 3.1). Third, the current model accounts for (self-equilibriating) steady torques (q) which provide a mechanism for tension detuning. Finally, the discretization employed in references [12, 13] differs from that used herein. The present description of longitudinal response (58) and (59) includes the rod rigid body modes (Φ_{10} and Φ_{20}), which are omitted in references [12, 13]. The effects of these differences are addressed in the examples of this and the following two subsections.

The current model is similar to that of references [12, 13] under the conditions of: (1) vanishing steady torque ($q = 0$); (2) small wheel moment and/or large steady end load ($m \ll 1$ and/or $n \gg 1 \rightarrow \theta_0 \simeq \bar{\theta}_0 \simeq 0$, $l \simeq \bar{l} = 1$); (3) vanishing support stiffness ($k = 0$); and (4) vanishing rod rigid body mode terms ($j = 1, 2, \ldots, H$ in equations (58) and (59)). The first four mode shapes computed under these conditions from the current model for the indicated stationary band/wheel system are illustrated in Figure 7. The small angle formed between the radial segments shown on the wheels illustrates the degree of rotational motion experienced in a particular vibration mode. Notice that the first and third (second and fourth) modes involve span deflections that are antisymmetric (symmetric) about the x axis and induce pure rotation (translation) of the left wheel, in agreement with the findings of reference [12].

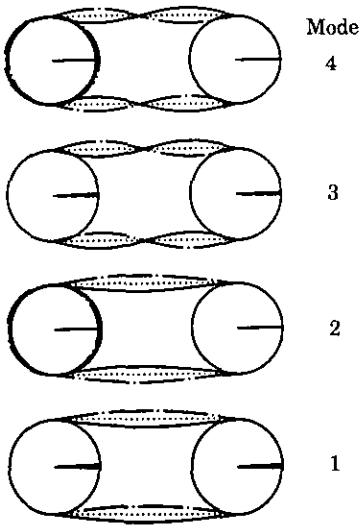

Figure 7. Comparison with the previous band/wheel model: the first four modes of the stationary band/wheel system having $m = 0{\cdot}0275$, $n = 28{\cdot}5$, $k = 0$, $i_1 = 32$ and $j_1 = j_2 = 1$. Equilibrium (· · · · · ·), and band at the beginning of (——) and mid-way (–·–·–) through one natural period of oscillation.

4.3. CONVERGENCE AND EFFECT OF ROD RIGID BODY MODES

Attention is focused on the rod rigid body mode terms, Φ_{10} and Φ_{20}, used in the current band/wheel model. In Figure 8 it is illustrated how these terms influence eigenvalue convergence for the indicated stationary band/wheel system. The solid (dashed) curves show the convergence of the first four eigenvalues when the rod rigid body modes are (are

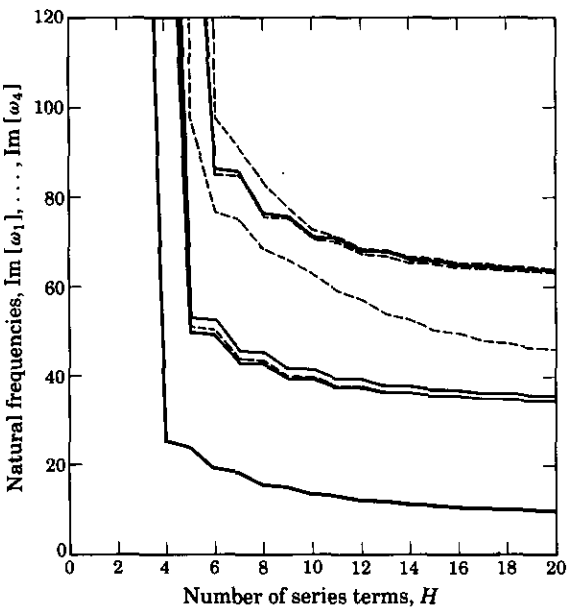

Figure 8. The effect of rod rigid body mode terms: convergence of the first four eigenvalues when the terms Φ_{10} and Φ_{20} are (——) and are not (– – – –) included in equations (58) and (59). In this example, $c = 0$, $m = 4$, $k = 0$, $q = 0$ and $n = 23{\cdot}4$.

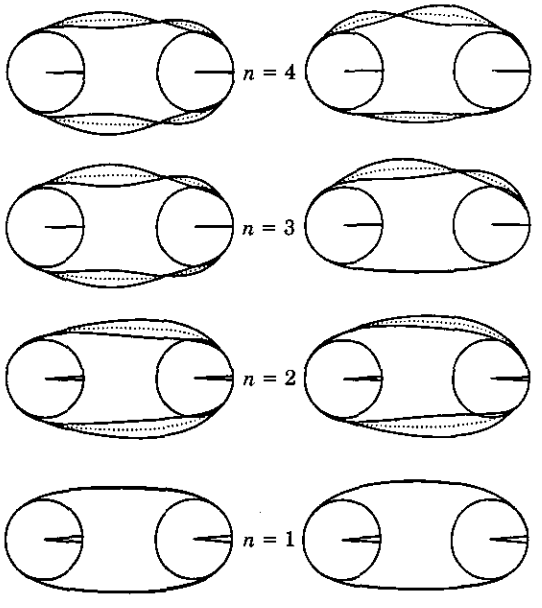

Figure 9. Mode shapes of the stationary band/wheel system. Results are shown for two cases; (a) $q = 0$ and (b) $q = 5$. (· · · ·), Equilibrium; (——), mode shape. In both cases, $m = 4$, $n = 23{\cdot}4$, $k = 0$, $i_1 = 100{\cdot}85$ and $j_1 = j_2 = 1{\cdot}745$.

not) included in the discretization. As shown in Figure 8, *including the rod rigid body terms improves the converge rate and leads to a "new" fundamental frequency*. The mode shape associated with this new fundamental natural frequency describes a *near rigid body mode* of the entire band/wheel system, and is discussed in the next section. Also, note that for the case in which the rod rigid body mode terms are included, the four eigenvalues have converged reasonably well for $H > 16$. Eigenvalue convergence was also tested for numerous other cases and, for the series size $H = 19$ employed in all examples to follow, the reported eigensolutions have converged fully.

4.4. STATIONARY BAND, $c = 0$

For future reference, a baseline system is defined by the following system parameters: $n = 23{\cdot}4$, $m = 4\,(r = \frac{1}{4})$, $c = 0$, $q = 0$, $k = 0$, $i_1 = 100{\cdot}85$ and $j_1 = j_2 = 1{\cdot}745$. These parameters, which correspond to those of the test stand described in section 5, describe a stationary ($c = 0$), symmetric ($q = 0$), free center ($k = 0$) band/wheel system with significant wheel inertia.

The first four modes for the baseline system are illustrated in Figure 9(a). The solid curves represent the mode shapes of the entire band/wheel system, and the dotted curves represent the equilibrium band profiles. Note that the mode shapes of the band have been enlarged for clarity. The fundamental mode ($n = 1$) represents a near rigid body mode, involving substantial wheel rotation and very little elastic deformation of the band. The second mode induces moderate rotation and light translation of the left wheel and elastic deformation of both bands. All higher modes are dominated by elastic band deformation and involve very small, though important, wheel rotations and translations.

The first six natural frequencies of vibration as the static load n is varied from the baseline case are shown in Figure 10. The second and higher order natural frequencies

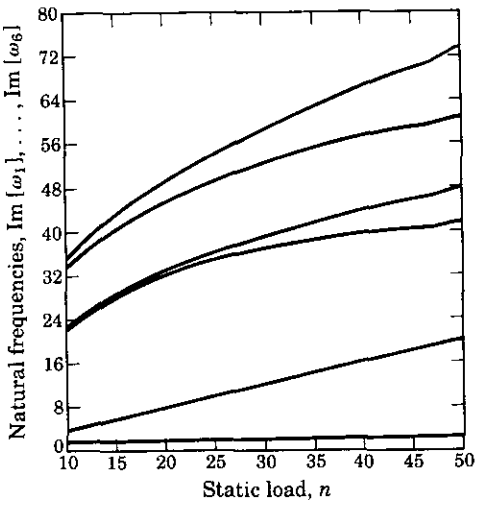

Figure 10. The effect of static load on the frequency spectrum for the stationary band/wheel system. The plot shows the first six natural frequencies of vibration for the case $c = 0$, $m = 4$, $k = 0$, $q = 0$, $i_1 = 100{\cdot}85$ and $j_1 = j_2 = 1{\cdot}745$.

increase rapidly with increasing static load due to the (membrane) stiffening of the upper and lower bands. However, this stiffening has little influence on the fundamental frequency, since the fundamental mode is a near rigid body mode involving little elastic band deformation (refer to Figure 9(a)).

Similarly, the fundamental frequency is largely insensitive to any static torque, q, as shown in the frequency spectrum in Figure 11. The static torque induces a tension difference between the bands, and this tension difference leads to stiffening of the lower (taut) span and softening of the upper (slack) span. These changes in static tension significantly influence the second and higher order modes involving elastic band deformation. For example, the first

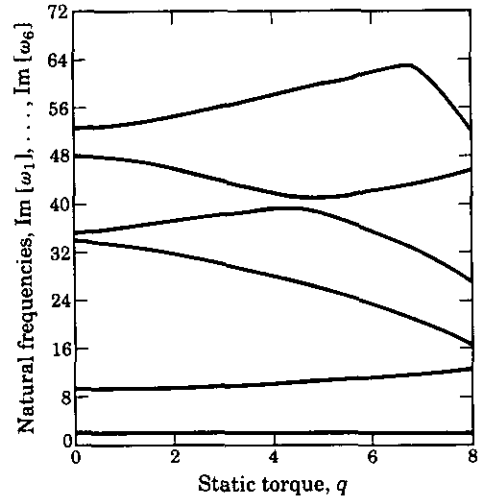

Figure 11. The effect of static load on the frequency spectrum for the stationary band/wheel system. The plot shows the first six natural frequencies of vibration for the case $c = 0$, $m = 4$, $k = 0$, $n = 23{\cdot}4$, $i_1 = 100{\cdot}85$ and $j_1 = j_2 = 1{\cdot}745$.

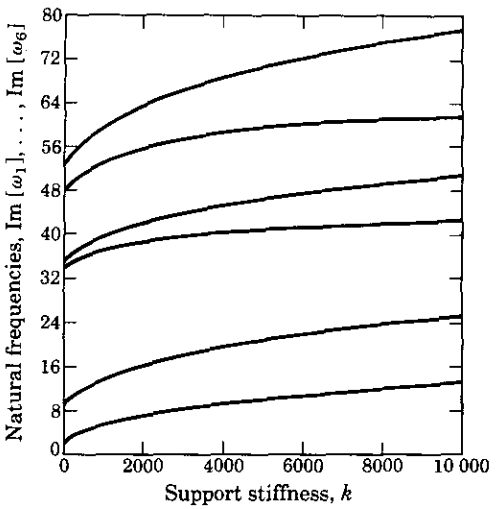

Figure 12. The effect of support stiffness on the frequency spectrum for the stationary band/wheel system. The plot shows the first six natural frequencies of vibration for the case $c = 0$, $m = 4$, $q = 0$, $n = 23{\cdot}4$, $i_1 = 100{\cdot}85$ and $j_1 = j_2 = 1{\cdot}745$.

four mode shapes for the case $q = 5$ are shown in Figure 9(b). Note that, like the band/wheel equilibrium, the modes are asymmetric (with respect to the x-axis) due to the tension and curvature detuning.

The fundamental mode is sensitive to increasing support stiffness as shown in the frequency spectrum in Figure 12, which illustrates the first six natural frequencies as the support stiffness is varied from the baseline case. Since all modes induce some translation of the left wheel, all the natural frequencies increase as the support stiffness increases.

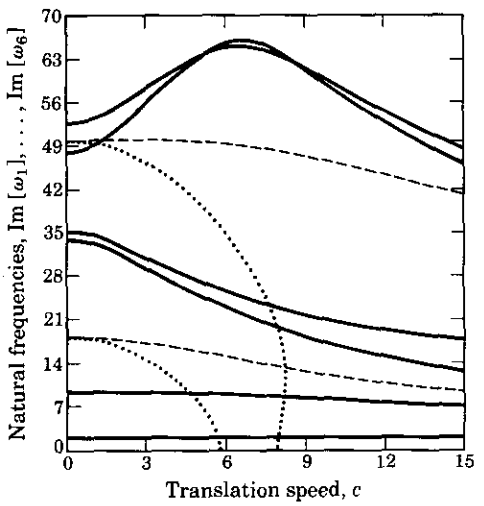

Figure 13. The stability of the band/wheel system: the first six natural frequencies *vs.* the translation speed for the band/wheel model (——); and the first two natural frequencies for the straight beam model with fixed support (· · · ·, $\eta = 0$) and free support (– – –, $\eta = 1$). For the band/wheel model, $m = 4$, $n = 23{\cdot}4$, $k = 0$, $q = 0$, $i_1 = 100{\cdot}85$ and $j_1 = j_2 = 1{\cdot}745$.

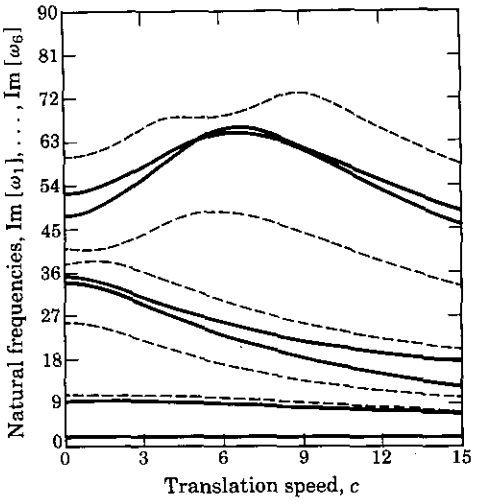

Figure 14. The effect of static torque q on the frequency spectrum for the translating band/wheel system: (a) (——), $q = 0$; (b) (– – –), $q = 5$. In both cases, $m = 4$, $n = 23{\cdot}4$, $k = 0$, $i_1 = 100{\cdot}85$ and $j_1 = j_2 = 1{\cdot}745$.

4.5. TRANSLATING BAND, $c \neq 0$

The stability of the translating band/wheel system at high translation speeds is now considered. The first six natural frequencies of vibration as the translation speed c is increased from the baseline case ($c = 10$) are shown in Figure 13. As discussed in section 4.1, the band tension increases with the translation speed and therefore influences the second and higher modes which induce elastic deformations. The fundamental natural frequency, however, is largely unaffected by the translation speed and maintains a near constant value. A comparison is made in Figure 13 with the natural frequency spectrum computed from the single straight beam model. Following references [3, 4], the first two natural frequencies are shown for the limiting cases of a fixed-center system ($\eta = 0$) and a free-center system ($\eta = 1$) for the same load n considered in the band/wheel model. For the case $\eta = 0$, the fundamental frequency vanishes at the first critical speed, signalling a divergence instability. No such instability exists for the free-center system ($\eta = 1$). In this case the stabilization derives from speed-induced band extension. By contrast, the speed-tensioning mechanism in the current mode develops from the equilibrium band curvature (see equations (31) and (32)). While both models predict substantially different frequencies (and modes), they both indicate that the band/wheel system can operate in a stable manner over the large speed range considered.

The addition of the applied torque q leads to tension detuning and may significantly alter the frequency spectrum, as seen in Figure 11 for a stationary band/wheel system. This effect is also observed in translating bands as seen in Figure 14, in which the frequency spectrum for the baseline case, $q = 0$, is compared to that for the case $q = 5$. Comparison of these two cases reveals that the torque preferentially stiffens those modes (numbers 2, 4, 6, . . .) that induce elastic deformation in the taut (lower) span (refer to Figure 9(b)). The frequencies of the odd order modes (numbers 3, 5, 7, . . .) decrease as they induce elastic deformation in the (relatively) slack upper span. Again, the static torque has little influence on the fundamental mode.

The free response of the translating band/wheel model ($c = 10$) is illustrated in Figure 15 for the two cases (a) $q = 0$ and (b) $q = 5$. The solid curves represent the free band/wheel response over a natural period of oscillation and the dotted curves represent the equilibrium band profiles. For the translating system, the free response has non-uniform

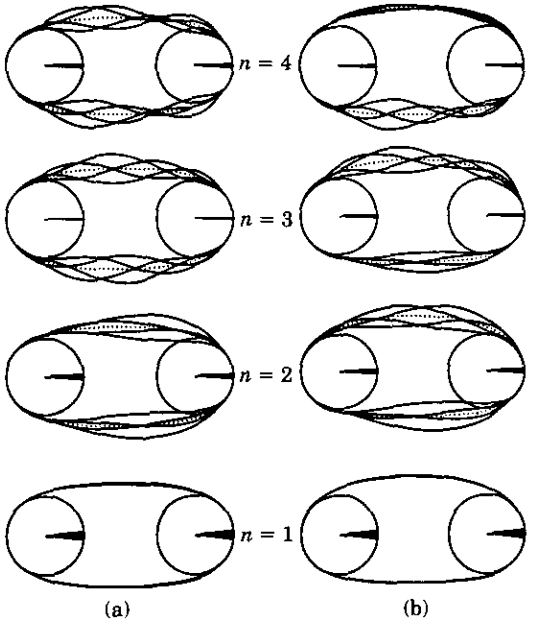

Figure 15. The free response of the translating band/wheel system at $c = 10$. Results are shown for two cases; (a) $q = 0$ and (b) $q = 5$. The band profile (——) is shown at times $t = 0$, $0{\cdot}25\tau$, $0{\cdot}5\tau$ and $0{\cdot}75\tau$, where τ is the associated natural period of oscillation. (· · · · ·), Equilibrium band profile. In both cases, $m = 4$, $n = 23{\cdot}4$, $k = 0$, $i_1 = 100{\cdot}85$ and $j_1 = j_2 = 1{\cdot}745$.

phase and is described by complex eigenfunctions. As with the stationary systems (Figure 9), the detuning generated by the applied torque q leads to an asymmetric band response for the translating system.

5. EXPERIMENTAL STUDY

An experimental study is performed to validate theoretical predictions of band/wheel system response. A schematic of the experimental apparatus is shown in Figure 16. The

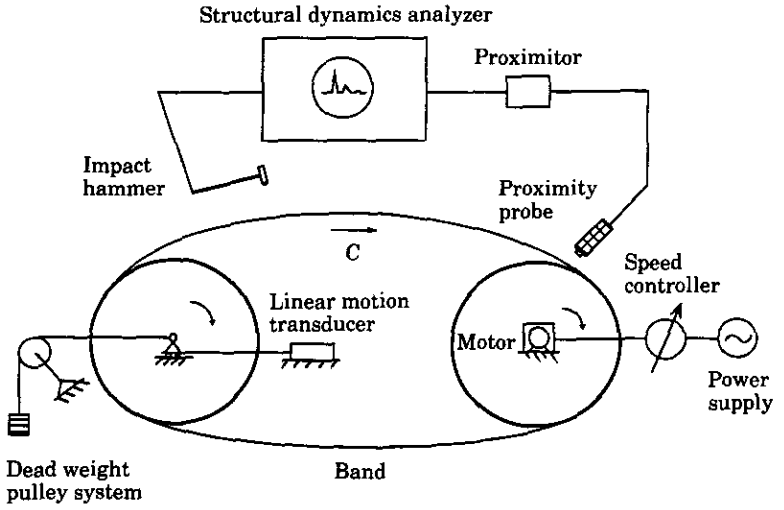

Figure 16. Schematic of band/wheel test stand and instrumentation.

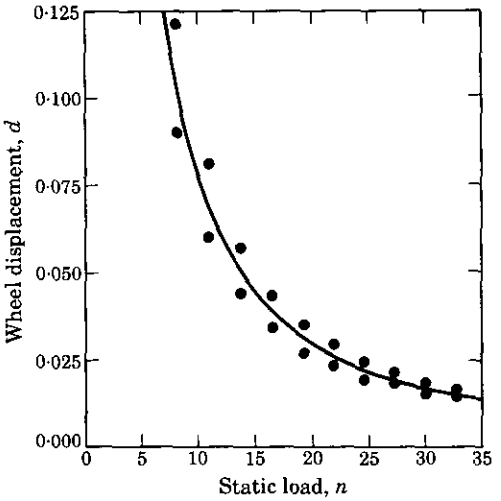

Figure 17. The experimental (•) and theoretical (——) static response of the left wheel. Baseline case; $q = 0$, $k = 0$ and $m = 4$ ($r = \frac{1}{4}$).

test stand consists of two (127 mm radius) wheels, a butt-welded steel band, a dead weight pulley system, and a (3 hp) d.c. motor. The right-hand wheel, the drive wheel, is stationary, whereas the left-hand wheel is free to translate horizontally on two linear motion guides. The dead weight pulley system, attached to the left-hand wheel, is used to adjust the span tension. The motor is equipped with a speed controller which provides controlled speeds in the range of 0–1750 rpm. The geometric and material properties of steel band are listed in Table 1. A linear motion transducer (potentiometer) detects the horizontal displacement of the left wheel. An impact hammer is used to excite lateral band vibrations, which are measured using a proximity probe near the right wheel. Force and response signals are recorded to disk on a structural dynamics analyzer (GenRad 2515), which performs standard signal processing functions.

5.1. STATIC RESPONSE MEASUREMENTS

Attention is first focused on the static response of the band/wheel system. The displacement d of the left wheel is measured for various applied loads n. A range of values of d are measured for a given load n due to the frictional forces acting on the linear motion guides. These frictional forces create a "dead band" in which small increments in n produced no increase in d. Although such variations exist, the experimental results agree with the theoretical predictions obtained from equations (42)–(44), as shown in Figure 17. For each of ten values of n, both high and low values of d are reported to indicate the total variation due to friction. This variation is greatest in the range of low static loads

TABLE 1

Band geometric and material properties

Steel band	Dimensions
Total length	1814 mm
Thickness	0·599 mm
Width	60·325 mm
Young's modulus	$2{\cdot}375 \times 10^{11}$ Pa
Density	7833·41 kg/m^3

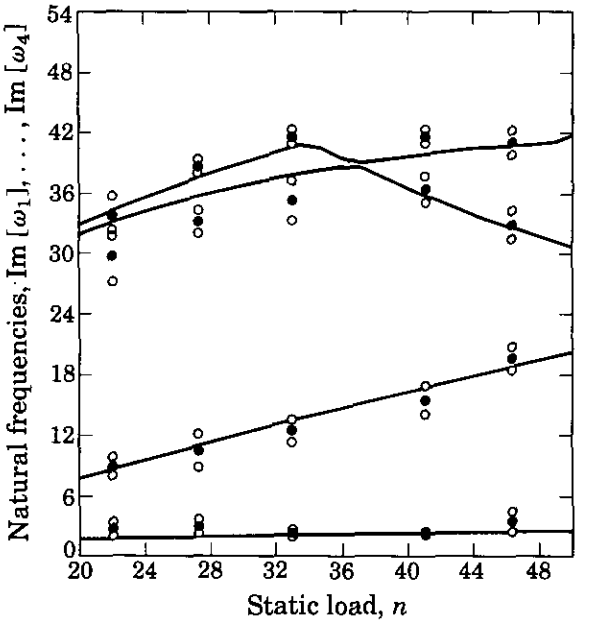

Figure 18. The experimental (o, •) and theoretical (——) natural frequencies for the stationary band/wheel system. Baseline case; $q = 0$, $k = 0$, $m = 4$ ($r = \frac{1}{4}$), $i_1 = 100{\cdot}85 + n(EI/\rho Ag(L^*)^3)$, where n is the static load due to the dead weight, and $j_1 = j_2 = 1{\cdot}745$. (•), Experimental average; (○), one standard deviation away from average.

where the frictional forces are a significant fraction of the applied load n. At higher static loads, this effect of friction diminishes. The system examined corresponds to the "baseline case" of section 3.1; a symmetric ($q = 0$), free center ($k = 0$), band/wheel system for which $m = 4$ ($r = \frac{1}{4}$).

Similar tests are performed to measure steady response when the band is translating. For a given static load, however, the position of the left wheel remains unaltered over the entire speed range $0 \leqslant C < 23{\cdot}94$ m/s. Thus the equilibrium geometry is observed to be independent of the translation speed in agreement with theory (refer to section 3). Note that, for a typical static load, $n = 33$, the highest speed $C = 23{\cdot}94$ m/s, corresponds to a non-dimensional speed of $c = 12{\cdot}75$, which is 221% of the critical speed, $c_{cr} = 6{\cdot}54$, defined by the fixed-center ($\eta = 0$) translating beam model [3–5].

5.2. DYNAMIC RESPONSE MEASUREMENTS

Dynamic characteristics of the band/wheel system are determined by measuring the natural frequency spectrum. The instrumented hammer is used to impact the band or wheel at locations selected to excite specific modes. For example, the elastic modes are best excited by impacting the bands near their mid-span. By contrast, lower order modes involving wheel translation and rotation are best excited by impacting the left-hand wheel directly. In these latter cases, a soft rubber tip is placed on the impact hammer to better excite the low frequency response. The proximity probe is positioned near the band/wheel contact point at the right-hand (stationary) wheel. Force and response signals are recorded by the structural dynamics analyzer and system (resonances) natural frequencies are determined from the computed transfer function. The transfer function was typically computed over a 32 Hz bandwidth.

The following preliminary observations are noted. The largest resonance corresponds to the fundamental *torsional* mode of the band; note the significant aspect ratio of the spans

(width/length = 12%). The torsional band response is unmodelled. The second mode is difficult to excite due to the large inertia of the left wheel. The dead weight, used to provide the static load, also contributes to the translational inertia of the left wheel. This additional inertia is included in the theoretical model by combining it with that of the left wheel.

The first four measured natural frequencies of the stationary band/wheel system, as a function of static load n, are shown in Figure 18. Five static loads in the (non-dimensional) range $20 \leqslant n \leqslant 50$ are used in the experiment. At each value of n, multiple tests were conducted and the average of each natural frequency (solid symbol) and one standard deviation about the average (open symbol) are reported in the figure. The solid curves, which represent the frequencies predicted by the band/wheel model, are generally within the range of the experimental values. In particular, note the good agreement between measured and predicted fundamental frequencies (near rigid body mode).

For the case of a translating band, several additional observations are made. The motor excitation frequency always corresponded to a peak in the measured transfer function in the range of obtainable motor rotation/frequencies (0–29·83 Hz). The passage of the butt weld connecting the ends of the continuous band also induced a peak in the transfer function at a known percentage of the motor frequency. The butt weld provides a dominant source of excitation, as observed in reference [13].

Qualitative experiments are performed to observe the stability of the band/wheel system while operating at high translation speeds. For reference, the intermediate static load value $n = 33$ is again used, and the classical critical speed for a fixed-center system ($\eta = 0$) is $c_{cr} = 6{\cdot}54$. During operation, the band/wheel system responds in a stable manner up to the maximum obtainable translation speed, $c = 12{\cdot}75$. Aside from resonances produced by the motor and weld frequencies, the band exhibits little dynamic response and maintains a stable (and constant) equilibrium shape.

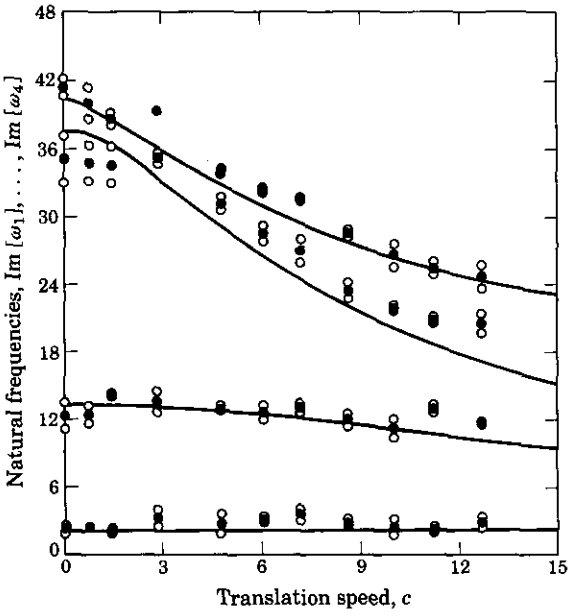

Figure 19. The experimental (○, •) and theoretical (——) natural frequencies of the translating band/wheel system for the case $q = 0$, $k = 0$, $n = 32{\cdot}936$, $m = 4$ ($r = \frac{1}{4}$), $i_1 = 100{\cdot}85 = n(EI/\rho Ag(L^*)^3)$, where n is the static load due to the dead weight, and $j_1 = j_2 = 1{\cdot}745$. (•), Experimental average; (○), one standard deviation away from average.

A quantitative experiment was performed on the above system to study how the natural frequency spectrum is affected by translation speed. The first four measured natural frequencies, as a function of translation speed c, are shown in Figure 19. Frequency measurements are made at ten translation speeds in the range $0 < c \leqslant 12{\cdot}75$. The solid curves, which show the frequencies predicted by the band/wheel model, are again in good agreement with the experimental values.

6. SUMMARY AND CONCLUSIONS

A theoretical model was derived that describes the non-linear, planar response of coupled band/wheel systems. The model, which considers geometrically large band deflections, is used for the analysis of system equilibrium (steady response), vibration and stability.

For the steady band/wheel response, the model describes a continuous elastica that is drawn under finite tension about two supporting wheels. An exact (elliptic integral) solution for non-linear steady response is derived for the equilibrium band curvature and tension. This solution is used to evaluate the equilibrium band geometry (speed independent) and tension (speed dependent) over a wide range of band/wheel designs and operating conditions. It is noted that: (1) the band partially unwraps from the supporting wheels ($\theta_0 \neq 0, \overline{\theta}_0 \neq 0$) as it buckles outwards under finite applied load n; (2) steady wheel torques destroy equilibrium symmetry ($\theta_0 \neq \overline{\theta}_0$) and lead to tension detuning; (3) the speed-induced tensioning results from equilibrium band curvature.

The equations of band/wheel motion are linearized about the equilibrium, and the linear response and stability are determined from the eigensolutions of a discretized model. The fundamental eigensolution describes a near rigid body mode dominated by in-phase wheel rotations. The second and higher order eigensolutions, which involve substantial elastic deformations of the band, are sensitive to all parameter changes leading to changes in band tension. In particular, the steady wheel torque has a significant influence on the band/wheel frequency spectrum and leads to asymmetric vibration modes. The results show that the band/wheel equilibrium remains stable at high translation speeds due to the aforementioned speed-tensioning effect.

A companion experimental study was performed to measure both the steady and dynamic response of band/wheel systems. Measurements of the steady wheel displacement are in very good agreement with theoretical values. Modal tests were performed to measure the natural frequencies of low order vibration modes over wide ranges of static loads and translation speeds. The overall agreement between the experimental and the theoretical frequency spectra supports the band/wheel model. Observations confirm that the band/wheel system maintains stability over the large range of translation speeds obtainable in the experiment.

ACKNOWLEDGMENTS

The authors gratefully acknowledge the support of the University of Michigan Office of the Vice President for Research and The University of Michigan Rackham Graduate School, and the partial support of the U.S. Office of Naval Research.

REFERENCES

1. C. D. MOTE, JR. 1972 *Shock and Vibration Digest* **4**(4), 2–11. Dynamic stability of axially moving materials.

2. J. A. WICKERT and C. D. MOTE, JR. 1988 *Shock and Vibration Digest* **20**(5), 3–13. Current research on the vibration and stability of axially-moving materials.
3. T. CHUBACHI 1957 *Bulletin of the Japan Society of Mechanical Engineers* **23**(127), 205–210. Lateral vibration of axially moving wire or belt form materials.
4. C. D. MOTE, JR. 1965 *Journal of the Franklin Institute* **279**, 430–444. A study of bandsaw vibrations.
5. A. SIMPSON 1973 *Journal of Mechanical Engineering Science* **15**(3), 159–164. Transverse modes and frequencies of beams translating between fixed end supports.
6. S.-J. HWANG and N. C. PERKINS 1990 *Proceedings of the CSME Mechanical Engineering Forum* **9**, 217–222. Nonlinear equilibrium analysis of axially moving materials.
7. N. C. PERKINS and S.-J. HWANG 1990 *Proceedings of the 31st AIAA Structures, Structural Dynamics and Materials Conference, AIAA-90-0942-CP, part* 4, 1979–1985. The stability of high-speed axially moving materials.
8. S.-J. HWANG and N. C. PERKINS 1992 *Journal of Sound and Vibration* **154**, 381–409. Super-critical stability of an axially moving beam; part I: model and equilibrium analysis; part II: vibration and stability analyses.
9. K. W. WANG 1991 *American Society of Mechanical Engineers, Journal of Vibration and Acoustics* **113**, 62–68. Dynamic stability analysis of high speed axially moving bands with end curvatures.
10. J. M. T. THOMPSON and T. S. LUNN 1981 *Journal of Sound and Vibration* **77**, 127–132. Static elastica formulations of a pipe conveying fluid.
11. C. D. MOTE, JR. and W. Z. WU 1985 *Journal of Sound and Vibration* **102**, 1–9. Vibration coupling in continuous belt and band systems.
12. K. W. WANG and C. D. MOTE, JR. 1986 *Journal of Sound and Vibration* **109**, 237–258. Vibration coupling analysis of band/wheel mechanical systems.
13. K. W. WANG and C. D. MOTE, JR. 1987 *Journal of Sound and Vibration* **115**, 203–216. Band/wheel system vibration under impulsive boundary excitation.
14. A. G. ULSOY 1986 *Journal of Vibration, Acoustics, Stress, and Reliability in Design* **108**, 207–212. Coupling between spans in the vibration of axially moving materials.
15. A. E. H. LOVE 1927 *A Treatise on the Mathematical Theory of Elasticity*. New York: Dover, 1944 reissue of fourth edition.
16. S.-J. HWANG 1991 *Ph.D. Dissertation, The University of Michigan, Ann Arbor, Michigan*. Super-critical stability of axially moving materials.
17. J. J. STOKER 1986 *Nonlinear Elasticity*. New York: Gordon and Breach.